Research Article Vol. 32, No. 23 / 4 Nov 2024 / Optics Express 41089

Optics EXPRESS

Xenon plasma-focused ion beam milling for fabrication of high-purity, bright single-photon sources operating in the C-band

MACIEJ JAWORSKI,[1,2] **PAWEŁ MROWIŃSKI,**[1,*] **MAREK G. MIKULICZ,**[1] **PAWEŁ HOLEWA,**[1,3,4] **LAURA ZEIDLER,**[1] **MARCIN SYPEREK,**[1] **ELIZAVETA SEMENOVA,**[3,4] **AND GRZEGORZ SĘK**[1]

[1] *Department of Experimental Physics, Faculty of Fundamental Problems of Technology, Wrocław University of Science and Technology, Wybrzeże Wyspiańskiego 27, 50-370 Wrocław, Poland*
[2] *Nanores, Bierutowska 57-59, 51-317 Wrocław, Poland*
[3] *DTU Electro, Technical University of Denmark, Kongens Lyngby 2800, Denmark*
[4] *NanoPhoton - Center for Nanophotonics, Technical University of Denmark, 2800 Kongens Lyngby, Denmark*
[*] *pawel.mrowinski@pwr.edu.pl*

Abstract: Electron beam lithography is a standard method for fabricating photonic micro and nanostructures around semiconductor quantum dots (QDs), which are crucial for efficient single and indistinguishable photon sources in quantum information processing. However, this technique is difficult for direct 3D control of the structure shape, complicating the design and enlarging the 2D footprint to suppress in-plane photon leakage while directing photons into the collecting lens aperture. Here, we present an alternative approach to employ xenon plasma-focused ion beam (Xe-PFIB) technology as a reliable method for the 3D shaping of photonic structures containing low-density self-assembled InAs/InP quantum dots emitting in the C-band range of the 3rd telecommunication window. The method is optimized to minimize the possible ion-beam-induced material degradation, which allows exploration of both non-deterministic and deterministic fabrication approaches, resulting in photonic structures naturally shaped as truncated cones. As a demonstration, we fabricate mesas using a heterogeneously integrated structure with a QD membrane atop an aluminum mirror and silicon substrate. Finite-difference time-domain simulations show that the angled sidewalls significantly increase the emission collection efficiency to approx. 0.9 for NA = 0.65. We demonstrate experimentally a high purity of pulsed single-photon emission (~99%) and a superior extraction efficiency value reported in the C-band of $\eta = 24 \pm 4\%$.

1. Introduction

In recent years, scientists worldwide have focused their efforts on studying single photon sources and their properties for emerging quantum technology applications. In this context, several competing approaches exist to generate non-classic light from solid-state systems, such as of low-dimensional semiconductors [1] or color centers in diamonds [2], Si, SiC or ion traps [3]. The subject of our research are semiconductor quantum dots (QDs), which are especially promising as they demonstrate several advantageous properties when compared to other solutions, including also the laser-based single photon sources. The most important are the ability to control the emission wavelength to match the telecommunication windows [4,5,6,7,8], triggered and on-demand emission of single photons [9], their high generation rates [10], and possible photonic

#534313
Journal © 2024
https://doi.org/10.1364/OE.534313
Received 1 Jul 2024; revised 7 Sep 2024; accepted 18 Sep 2024; published 28 Oct 2024

chip integration with the use of QD localization [11] and deterministic processing [12,13,14]. The on-demand generation of single photons with high emission purity and brightness is desirable for potential applications in quantum communication and quantum computing schemes [15]. They promise the realization of scalable quantum photonic integrated circuits [16] and have been demonstrated in quantum key distribution for secured communication networks [17], where low multiphoton contribution and the coherence in the emitted photon-number states provide additional security benefits [18,19].

Efficient on-demand generation of single photons requires the fabrication of photonic microstructures containing deterministically integrated QD. A proper design shall offer directionality of emission, improving the photon extraction efficiency (η) [20], or simultaneously, as in the case of resonant cavities, acceleration of spontaneous emission rate due to the Purcell effect [21]. In addition, the ideal spectral range of single-photon emitters for applications in optical fiber networks would be the telecom C band due to the minimum of the optical signal attenuation. InAs QDs grown on InP are among the leading material system candidates, which have been proven to be easily tunable to the wavelength of 1.55 µm [22,6,23,24,25]. The commonly used approach for fabricating photonic structures employs electron beam lithography (EBL) combined with etching, which, however, has some drawbacks. For instance, the EBL processing requires using electron resists layers deposition very often still combined with conventional masks, process, which complicates the processing. Although even more advanced in-situ EBL in combination with cathodoluminescence technique allows shaping microstructures like monolithically integrated microlenses [26], compared to that the FIB milling is a one-step process which is a significantly simpler technology [27]. Therefore, an interesting alternative is based on using a double-beam scanning electron microscope/focused ion beam (SEM/FIB) system to process photonic microstructures, which has already been proven successful for GaAs-based [28] and GaN-based [29] quantum dot structures. Here, we extended the capabilities of this technology to more application-relevant systems with InAs/InP QDs as the emitters, integrated additionally with the silicon platform, towards efficient, telecom single photon sources obtained deterministically in a simple and cost-effective technology prepared to order.

The SEM/FIB system contains an electron beam column for high-resolution imaging and an ion beam column for three-dimensional milling. Typically, this configuration is used in the sample preparation process for transmission electron microscopy (TEM) or failure analysis [30,31], as this is a maskless and direct method, which makes it optimal for prototyping in a fast and cost-effective manner. Additionally, this method can be used to fabricate photonic microstructures around quantum emitters, although the negative effect of incident ions causing defects in the crystal structure along incident and lateral dimensions must still be considered [32]. To counteract the negative effects of the ion beam on the crystal lattice, the demonstrations have concerned so far mostly QDs placed in the micro-cavity defined by the distributed Bragg reflectors (DBR), which at the same time protected the dots against the ion bombardment by a multilayer material with a total thickness of above 1.5 µm [33,34]. On the other hand, using DBR-based cavity structures makes the growth complex and expensive. Although such configuration is able to offer high extraction efficiency, its disadvantage is spectrally narrow photonic mode, which requires very precise spectral matching with the QD emission lines. On the other end, there are photonic confinement structures in a form of mesas or microlenses, which use much thinner capping and offer a good compromise between the maximal extraction efficiency and its spectral broadening – the latter being at least an order of magnitude larger than for microcavities. Therefore, our focus revolved around structures with thinner cap layers, which simplifies the growth technology and simultaneously allows obtaining spectrally broad extraction efficiency, especially advantageous when dealing with strongly inhomogeneous QD ensembles [32,28].

This study demonstrates both non-deterministic and deterministic approaches to the fabrication of micrometer-sized photonic structures in the form of mesas containing self-assembled QDs used as non-classical photon states generators for quantum technology applications. The mesas are defined in a one-step process by the xenon plasma focused ion beam (Xe-PFIB), allowing for fast (2.5 min.), nanometer-precision milling of mesa structures around the optically located InAs/InP QDs, emitting in the telecom C-band. We show that the Xe-PFIB fabricated photon emitter reveals high single-photon purity (low multiphoton probability) in triggered operation under driving by a sequence of optical pulses with 76 MHz frequency. Furthermore, the positioning of a QD in a mesa by PL imaging, combined with the presence of the metallic mirror beneath the mesa, lead to increased source brightness due to the photonic confinement induced directionality in a broad spectral range.

2. Fabrication – QD structure and Xe-PFIB processing

The QD sample was grown by low pressure metalorganic vapor phase epitaxy (MOVPE). The self-assembled InAs/InP QDs were formed in the Stranski-Krastanov growth mode [25] and embedded in a 580 nm-thick InP. The resulting QD array possesses a low surface density of QDs ($\sim 2.8 \times 10^9$ cm^{-2}) emitting in a wavelength range from 1.5 to 1.6 µm. The wafer is coated by plasma-enhanced chemical vapor deposition with a 603 nm thick SiO_2 layer and subsequentially with 130 nm of Al from the electron-beam evaporator. The QDs wafer is then bonded to an Si wafer using benzocyclobutene (BCB) adhesive layer. The InP substrate is removed in the HCl bath, whereas the InGaAs sacrificial layer is removed in (10%)H_2SO_4:H_2O_2:$H_2O = 1{:}8{:}80$ solution. The bonding procedure is performed at 250°C in vacuum under the applied mechanical force of approximately 2 kN.

Mesas of different sizes were processed by the Xe-PFIB. The Xe ions are indifferent with the lack of electron affinity to III/V elements [35,36]. On the other hand, the Xe-PFIB technique increases surface amorphization due to the high redeposition rate of the material, however, the resulting roughness is composed of artifacts of below 40 nm size, which does not have a detrimental effect on the final shape and size of the few microns large structures [28]. Additionally, the beam spot size for the xenon source is greater than for gallium and depends strictly on the energy and current of the beam. For example, for the 1 nA beam current, the spot size (φ) is expected to be at most 150 nm large, and together with fixed overlap (σ) of the successive spots of 50% [37], gives that the milled area is uniformly exposed to the beam ions [38].

The scheme of the sample structure milling is schematically depicted in Fig. 1(a). The ion beam energy was set to the lowest available value of 10 keV, which minimizes the structure degradation upon ion beam exposure. Thus, the radiative recombination from quantum dots is not diminished, allowing a one-step maskless approach using no protective layers. Based on our previous experience [28,39], we optimized the process in terms of the fabrication time, resolution, as well as the structural and optical quality of the milled photonic structures. We found the optimal beam current at 1 nA and dwell time of 1 µs. [28] This combination of parameters enabled to fabricate mesas within approx. 2.5 min. In Fig. 1(b), we demonstrate an SEM image of the milled mesa with angled sidewalls with a bottom diameter of about $D = 3.5$ µm and a height of $h = 580$ nm. We used an inner-to-outer milling mode in a basic ring pattern with fixed inner and outer diameters (the outer field diameter is about 16 µm). Furthermore, we successfully created an array of 30 mesas, which differed only in the bottom diameter (D) of approximately 2.0 µm, 3.5 µm, and 5.0 µm, while the top diameter (d) is typically lower by approx. 0.6 µm. This shape can be related to the profile of the ion beam and can be controlled by the ion beam energy and beam current to some extent.

In a non-deterministic approach, the array of microstructures are milled, and depending on the areal density, there is some probability to find photonic structures with a well-centered single QD. Therefore, the presented Xe-PFIB methodology has also been used deterministically, where the dot is preselected first by a photoluminescence (PL) mapping (see description in Section 5).

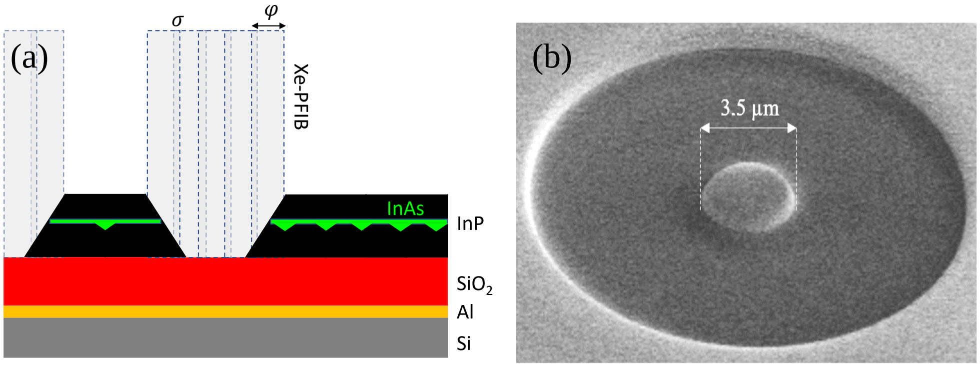

Fig. 1. a) Schematically presented layout of the sample processed by the focused ion beam. The milling is characterized by a beam diameter (φ~150 nm) and overlap (σ=50%) of the beam during milling. In this fabrication scheme, the mesa has a truncated cone shape with *d* as the top diameter, *h* as height, and *D* as the bottom diameter. b) (a) Xe-PFIB-milled mesa inspected by the scanning electron microscope in the double-beam system.

Thus, the QD position is known, and the photonic microstructure could be fabricated at its exact position.

3. FDTD simulation results

The angled sidewalls in the truncated cone shape of the mesa microstructures realized by the Xe-PFIB are favorable for increased extraction efficiency due to the refraction of light towards the collecting lens [40–42]. We performed FDTD simulations for this specific mesa geometry to provide more insight into the case of InP-based microstructures on thick SiO_2 and Al mirror, focusing mainly on the light collection in the out-of-plane direction. The simulations are performed for a point-like dipole emitter situated in the center of an InP mesa, resolving the spectral range from 1.4 to 1.7 µm. We begin with the optimization scan for the mesa bottom diameter, focusing on the extraction efficiency within 40 deg. angle cone of the detection system (40 deg. corresponds to NA = 0.65 of a microscope objective commonly used in µPL experiments, also in the measurements here – see the following subsection) for the dipole emission around 1.55 µm wavelength. The results are shown in Fig. 2(a). Due to the bottom metallic mirror, we can see that for the whole range of probed sizes, the extraction efficiency (η) is expected to be not less than η = 0.15, typically much higher, reaching even η ≅ 0.90 for a 4 µm-in-diameter mesa [43]. The presence of the pronounced maximum originates from the constant inclination of the wall as the mesa diameter is changed The weak-cavity design in our mesas shows relatively moderate Purcell enhancement, usually not exceeding 2, i.e., significantly lower than for the high-Q cavity systems, both in-plane [44] or vertical, with top and bottom mirrors [45]. We also note regularly spaced minima, corresponding to mesa diameter 3.4, 3.8, 4.3, 4.8 and 5.3 µm. A complex field scattering in 3D weak-cavity could result in diverging of the dipole emission along the in-plane directions for these particular geometries.

The high-Q cavities, with their ability to provide η of more than 0.8, offer a practical solution for achieving high coupling efficiency to an external single-mode fiber via the cavity resonant mode. Despite the mesa geometry not yielding high-Q factors, we can still achieve increased extraction efficiency. This is possible due to photonic-confinement-driven emission directionality, especially when combined with high numerical aperture collection optics (microscope objective in the free space or large NA fiber directly bonded to the mesa) [7]. This approach is not

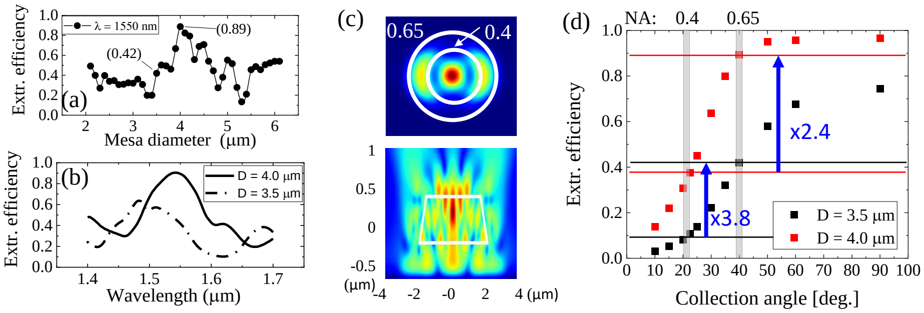

Fig. 2. (a) Calculated extraction efficiency (η, NA = 0.65) for photonic microstructures at 1.55 μm wavelength varying the bottom mesa diameter, and (b) wavelength dependence of the specific mesa with 4 and 3.5 μm in diameters. (c) Field distributions |E| for 4 μm size mesa at 1.55 μm wavelength showing far-field distribution (upper panel) along the normal direction and cross-sectional near-field distribution in the mesa (lower panel). (d) Extraction efficiency dependence in function of collection angle of the detection lens. Blue arrows indicate significant improvement for collected emission including refracted light related to the side peaks as seen in the far-field.

limited to the narrow spectral range [42], which is one of the main advantages of such a solution. The full spectrum of results for NA = 0.65 and both $D = 4.0$ μm and $D = 3.5$ μm mesa size is presented in Fig. 2(b). In the first case, a broadband improvement of photon extraction is expected ($\eta > 0.6$ for more than 80 nm spectral range) with the peak maximum of $\eta \cong 0.90$. The optical field distribution in the cross-section and the far-field pattern, presented in Fig. 2(c) implies improvement of extraction efficiency due to angled sidewalls, which refract the in-plane dipole emission towards the out-of-plane direction manifested by the additional side-peaks in the far-field. It is worth noting that by using a microscope objective with NA = 0.4, the "side peaks" collection is limited, resulting in 2.4 times reduced extraction at 1.55 μm (see Fig. 2(d)). Considering the mesa of 3.5 μm in diameter corresponding to the fabricated one, the calculated value for NA = 0.65 is $\eta = 0.42$ at 1.55 μm wavelength (for NA = 0.4, the η is 3.8 times lower), and its spectral dependence shows a maximum ($\eta > 0.6$) at slightly shorter wavelengths around 1.48 μm (see Fig. 2(b)).

4. Spectroscopic results

To evaluate the impact of the mesa-milling process on the QD emission properties and photon extraction efficiency, we performed high spatial resolutions photoluminescence measurements (μPL) at cryogenic temperature (7 K). The samples were mounted on a copper cold finger in a liquid-helium-flow cryostat and excited by a continuous-wave (CW) semiconductor laser diode at 660 nm. A 0.65 numerical aperture infinity-corrected microscope objective with ×50 magnification provided the excitation and emission collection. The collected photons were spectrally analyzed in the 0.5-m focal-length monochromator using a 600-grooves/mm grating and a multichannel liquid-nitrogen-cooled InGaAs linear detector. The μPL setup with monochromator gives a spectral resolution of ~25 μeV and a spatial resolution of ~2 μm, allowing for spectrally isolating single QDs and exciting a single mesa structure, while the detection based on tunable fiber optic filtering is limited by a bandwidth (full width at half maximum) of 15 μeV (0.3 nm). The same filtering system is used for all-fiber-based Hanbury-Brown and Twiss (HBT) interferometer to probe single photon emission purity from a QD via measuring the second-order correlation function. Photons of emission lines matching the filter-selected band enter a time-correlated single photon counting system using two NbN superconducting nanowire single-photon detectors (SNSPD). Such detection provides ~40 ps temporal resolution and ~60% photon detection efficiency at 1550 nm wavelength. The histograms are recorded with the time bin of 100 ps.

Near-infrared PL imaging for QDs positioning before the FIB milling is realized in a wide-field microscope configuration with a 2D thermo-electrically cooled InGaAs camera. The 660 nm CW laser uniformly illuminates the sample surface of more than (50×50) µm^2 to excite the QD emission. For that, the laser beam is shaped by the beam expander and focused on the backside of the microscope objective. The PL image is collected by the same objective and transmitted through a spectral filtering system: a 1.2 µm or 1.5 µm long-pass filter followed by a bandpass filter centered at 1.55 µm with the 15 nm or 3 nm full width at half maximum. The QD localization is determined in the image post-processing, similar to the method described in more detail in Ref. [14], elaborated with an additional denoising via cross-correlation of the PL map with the 2D Gaussian peak. The setup magnifies the illuminated area 200 times, allowing the recording of the field of ~250 µm^2. The spatial uncertainty of the emitting point peak position is ~100 nm.

To ascertain the photon extraction efficiency of the investigated QD (η_{QD}), we adopt the approach using tunable laser focused on the mirror mounted in the sample space [42]. The laser in the setup was tuned to the 1560 nm (within the emission range of the QD under investigation). The laser's intensity was decreased using neutral density filters (to avoid saturation of the detector) to attain a count rate in the megahertz (MHz) range on the superconducting nanowire single-photon detector (SNSPD). This count rate is adjusted considering factors such as the mirror's reflectivity (97%), filter attenuation, transmission through the cryostat window (90%), and the microscope objective (50%). The setup efficiency measured for a reflected laser is given for a well-focused spot which is almost ideally coupled to a single mode fiber via aspheric lens of NA = 0.15. Based on the laser power incident on the silver mirror, the estimated setup efficiency is found to be $\eta_{Setup} = (0.36 \pm 0.05)$ %, where the uncertainty, represented by the standard deviation σ(η), primarily arises from minor variations in the efficiency of fiber in-coupling across different wavelengths. However, in the case of the mesa emission we should consider less than ideal coupling to the single mode fiber, due to mismatch of acceptance angle, i.e. etendue of the optical system related to the source(detector) diameter and the numerical apertures of collecting(focusing) lenses. In this sense, the source diameter can be approximated by the mesa diameter of $D = 3.5$ µm and the detector diameter is a fiber core diameter of $d_{core} = 8.2$ µm, while the collection(detection) is realized via NA = 0.65(0.15) optics. The ratio of etendue ($\varepsilon = S\pi \mathrm{NA}^2$, $S = \pi d^2/4$) for these optical systems is given by $\varepsilon_{det}/\varepsilon_{col} = 0.29$. Including this additional limitation for transferring photons from the mesa to SNSPD via optical fiber we end up with $\eta_{Setup,mesa} = \eta_{Setup}\varepsilon_{det}/\varepsilon_{col} = 0.1\%$. In other words, the 0.36% of setup efficiency translates to hitting the SNSPD only with the central peak observed in the far-field within the NA = 0.4, while to evaluate extraction efficiency to the first lens including side peaks for NA > 0.4, the setup efficiency is 0.1%.

To experimentally estimate photon extraction efficiency from a mesa, it is necessary to identify emission lines from a single QD in the target spectral range. Exemplary µPL results are presented in Fig. 3, tackling the selected non-deterministic mesa structure with a diameter of 3.5 µm. The spectra in Fig. 3(a), recorded for various excitation powers, give an insight into the fundamental excitonic states of a single QD emitting near the 1.55 µm wavelength within this mesa. At low excitation power, the mesa response consists of two main, well-isolated, high-intensity lines. The linear polarization-resolved experiment (Fig. 3(b)) revealed that the line at ~1557 nm exhibits significant polarization splitting of ~74 µeV, suggesting the presence of the fine structure, typical for neutral exciton (X) in a QD affected by some potential confinement anisotropy [46]. With increasing the excitation power, a new line appears at ~1563 nm, i.e., at lower energy - this line has the same linear polarization splitting of ~74 µeV. Moreover, the splitting phase is orthogonal to that observed for the line at ~1557 nm (Fig. 3(a)), which allows us to interpret the longer wavelength one as related to emission from a biexciton state (XX) of the same QD. Hence, the XX binding energy could be estimated to be 3.3 meV, which might be considered as typical for QDs of InAs on InP system [46,6,47].

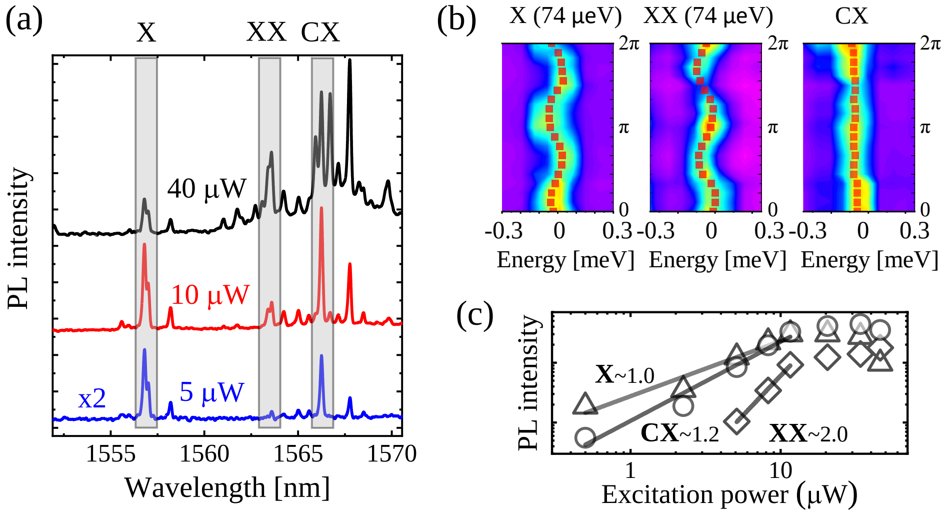

Fig. 3. (a) High-spatially resolved photoluminescence (μPL) spectra registered at different excitation power (P_{exc}) for the selected mesa in the spectral window near 1550 nm. (b) Spectral evolution of the X, XX, and CX lines, labeled as in (a), as a function of detected linear polarization. The numbers indicate the value of the fine structure splitting for the X and XX lines. (c) Power-dependence of the μPL intensity for the selected spectral lines. The numbers indicate the exponent in the fitted power function ($I \propto P^{\alpha}$), which is shown by the solid straight line.

In the low-excitation spectrum, the second intensive single line can be seen at ~1566 nm, which does not exhibit any splitting in the polarization-resolved experiment (see Fig. 3(b)), suggesting the spin singlet nature of the recombining state linked to the charged exciton (CX) recombination. The energy separation from the neutral exciton line is approx. 4.7 meV, therefore comparable to the negatively charged exciton binding energy in an InAs/InP QD [47,46].

The assignment of the spectral lines' origin is additionally supported by the analysis of their intensity (I) evolution with the increasing excitation power (P_{exc}) presented in Fig. 3(c). We observe a nearly linear emission intensity increase for the X line ($I \propto P_{\mathrm{exc}}{}^{1}$) and almost quadratic for the XX one ($I \propto P_{\mathrm{exc}}{}^{2}$). Such intensity dependence fits a few-level kinetic rate equation model for the occupation of the X and XX states in a single QD, providing the exciton/biexciton lifetime ratio of ~2 [48,49]. At the same time, the CX line intensity evolution gives $I \propto P_{\mathrm{exc}}{}^{1.2}$, with an exponent value slightly larger than one, also typical for charged excitons. One can notice that for elevated P_{exc}, more spectral features appear in the μPL spectra, especially in the 1562 -1570 nm range, contributing to a background emission for the selected XX and CX lines. This background appearance can be attributed to the recombination of higher exciton complexes in the investigated QD or can come from other QDs enclosed within the same mesa structure (located less centrally). However, to estimate photon extraction efficiency, the excitation power can be kept low enough to effectively eliminate the background photons from the photon number statistics.

We meticulously tested the possibility of single photon emission from a QD in a mesa. The second order correlation function was determined for the X state under the non-resonant (660 nm) CW excitation. In Fig. 4(a), one can see the spectrum of the QD emission after it was coupled to a single-mode fiber, passed through a tunable fiber optic filtering system, and then recorded by an SNSPD. The spectrum was captured at low excitation power conditions ($P_{exc} < 10$ μW) and the chosen X emission exhibited a low background counts level on the order of 50 Hz, which is highly desirable for minimizing the contribution of multiphoton coincidences. To measure photon statistics in the HBT interferometer, the X emission was filtered out from the spectrum and transmitted through the 1:2 fiber optic coupler ended by two SNSPDs. The recorded autocorrelation histogram, as shown in Fig. 4(b), demonstrates high purity of single photon emission. Here we used Gauss curve fitting, which in the proximity of the antibunching dip corresponds well to convolution of the exponential and Gaussian function to include timing jitter. The minimum of the antibunching dip and with the standard error propagation method we obtain $g^{(2)}(0) = 0.04^{+0.08}_{-0.04}$. In addition, we observe no coincidences at zero time delay within the entire ca. two hours of the histogram collection (see the inset of Fig. 4(b)).

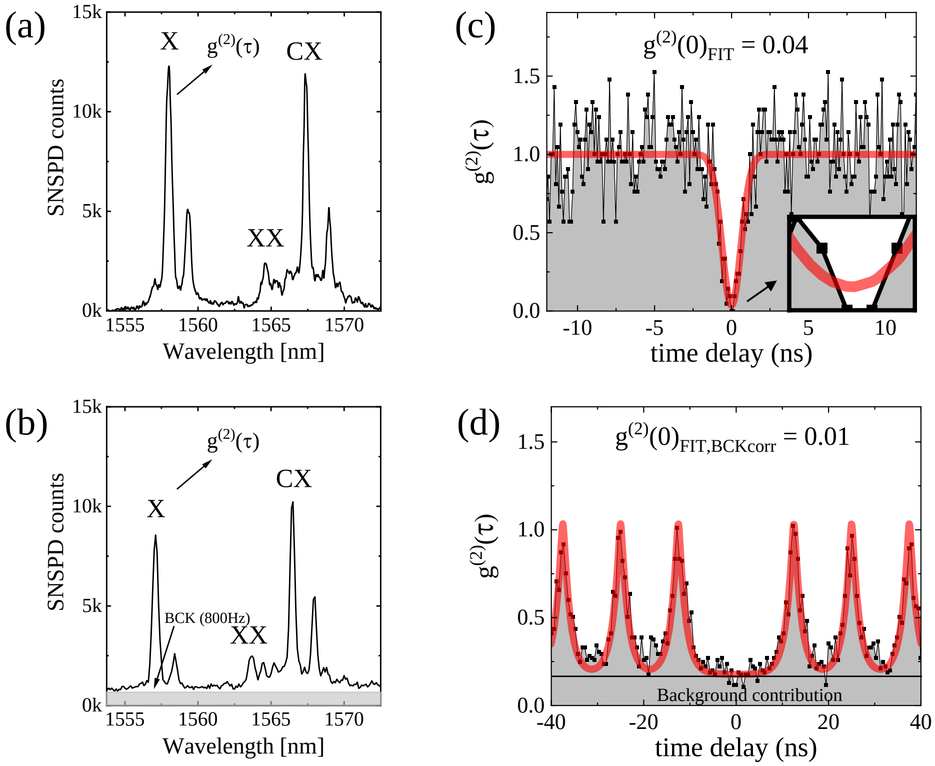

Fig. 4. Quantum dot spectra from a non-deterministic mesa structure realized by Xe-PFIB under (a) continuous wave 660 nm and (c) pulsed 805 nm excitation, and the respective autocorrelation histograms (b,d) showing high suppression of multiphoton events at zero time delay of 0.04 and 0.01, respectively.

Next, the photon autocorrelation was measured in the pulse excitation regime, i.e. a triggered mode. The QD was excited by ~50 ps-long optical pulses with a 76 MHz repetition frequency at 805 nm and an average power of 100 μW. The resulting μPL spectrum is presented in Fig. 4(c), showing ~8 kHz counts of the X emission, ~10 kHz counts of the CX emission and around 1.5 kHz counts for the XX line. Figure 4(d) displays the registered autocorrelation histogram in the HBT experiment for the X line. Here, we observe inevitable background coincidences originating from the background emission seen in the SNSPD spectra on the level of ~800 Hz. Therefore, the evaluation of X emission purity under pulsed excitation takes into account signal (~8kHz) to background (~800 Hz) ratio $\rho = s/(s + b) = 0.91$ and the related background $g^2(\tau)$ contribution of $1\text{-}\rho^2 = 0.17$, which results in background-corrected purity of the source of ~0.01 [50]. While raw data reveals $g^{(2)}(0)$ ~0.18, the fitting performed with the exponential function convoluted with a Gaussian to take into account timing resolution of 50 ps, results in $g^{(2)}(0) = 0.18 \pm 0.03$, and so the background corrected result reads $0.01^{+0.03}_{-0.01}$.

After estimating the count rates for selected QD emission lines and the background counts under the optical pulse driving, we could estimate the extraction efficiency. At these excitation conditions (low excitation power), two main competitive recombination channels, X and CX, are observed, with negligible contributions from the XX (see Fig. 4(c)) indicating low pumping rate. Therefore, using the all-fiber setup, we use the sum of X and CX SNSPD counts to evaluate the photon extraction efficiency (η_{exp}) from a single QD. This translates to $\eta_{\text{exp}} = \frac{18kHz}{76MHz \cdot 0.1\%} = 0.24 \pm 0.04$ (uncertainty of 4% comes mainly from the measured transmission of the optical elements in the standard error propagation evaluation). These estimates have been taken with (0.10±0.03)% setup efficiency for the NA = 0.65, assuming perfect QD internal quantum efficiency. Apparently, the η_{exp} is less than the calculated one ($\eta = 0.42$) for this mesa geometry. The difference can be attributed to the QD position shifted from the mesa center or not having an ideal QD internal quantum efficiency influenced due non-radiative losses [51,52]. However, the most significant finding is the obtained 24±4% extraction efficiency from an InAs/InP QD emitting at nearly 1550 nm enclosed within the FIB-fabricated mesa, which presents a superior result. This is almost two times overcoming the previously obtained η_{exp} of ~13% (NA = 0.4) for a planar QD structure on a distributed Bragg reflector [22] and 17% (NA = 0.4 [14], NA = 0.6 [10]) for a QD coupled to a circular Bragg grating, and similar to the very recent demonstration of a record value of 24% from elliptical Bragg grating [53] which indicates the potential of the approach used here.

5. Deterministic fabrication of photonic mesa structures

The FIB milling method for making the QD-based devices can be efficiently combined with pre-selection of the QDs from a planar structure by, e.g., a fast optical imaging technique. [13,14]. Here, we show that such a combination paves the way towards rapid and cost-effective deterministic fabrication of bright QD-based single photon sources for the example of application-relevant 1550 nm wavelength range. The same planar structure with InAs/InP QDs on silicon was processed in the Xe-PFIB with a high-energy beam to fabricate alignment marks on the structure's surface, defining areas of 20×30 μm^2 grouped into several blocks. The QD preselection requires a few steps, so we collected each field in sequence PL images for 1200 nm long pass (LP) filtering only and for both 1500 nm LP filter and 1550 ± 7.5 nm or 1550 ± 1.5 nm band-pass filter. The respective images are presented in Figs. 5(a-c). First, we clearly identify alignment marks taking advantage of strong emission of 2D layer states [54–56] around the 1250 nm wavelength range, which overwhelms the QD emission, resulting in a smooth intensity distribution in the planar region and pronounced light scattering on the markers. Secondly, the spectral filtering above 1500 nm is used to retain the QD emission (Fig. 5(b) and 5(c)), while the additional bandpass filtering allows to observe only those emitting around the target 1550 nm wavelength. The pronounced 2D Gaussian-like peaks were observed in the given field of view, and its center position with respect to the alignment marks is used for deterministic processing (accuracy of the QD position with respect to alignment marks is ~1 μm, which results from the temporal stability of the setup within the 30 second of measurement). Next, we validate the spectra from the isolated QDs by collecting the μPL on these bright spots using confocal filtering on the 100 μm pinhole. The sample is then processed by Xe-PFIB to fabricate mesas in the specific positions. In this way, we made two mesas on the field with deterministically integrated QDs (QD1 and QD2), as shown in Fig. 5(d).

To provide additional insight into the quality of deterministic processing using Xe-PFIB, we plot μPL spectra for each individual mesa before and after fabrication. First, one can notice that

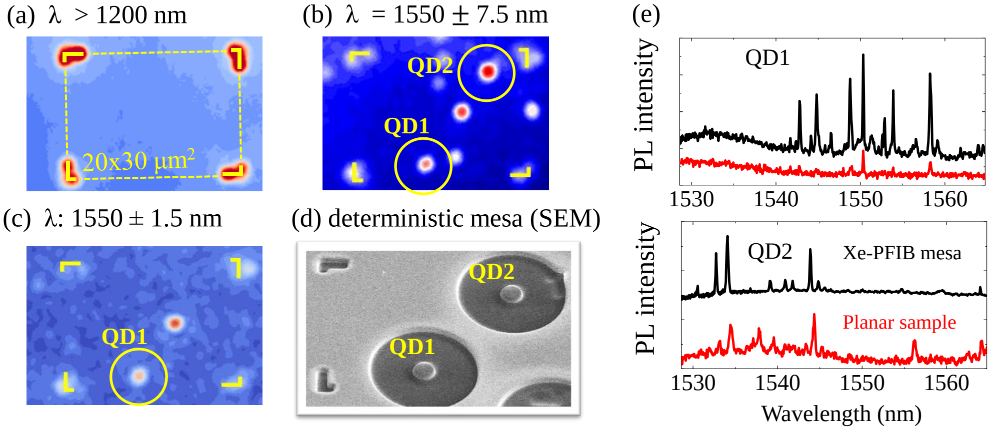

Fig. 5. (a) Photoluminescence wide-field imaging of planar samples using (a) long pass filtering of 1200 nm, (b,c) long pass filtering of 1500 nm together with bandpass filtering centered at 1550 with (b) 15 nm band and (c) 3 nm band. (d) Deterministically fabricated mesas at QD positions found in (b). (e) Microphotoluminescence spectra of QDs were selected from the PL image in (b) before and after mesa processing.

in the given spectral range, the emission pattern looks similar for fabricated mesas before and after fabrication, implying no degradation of the crystal structure in the vicinity of the emitter. In the case of QD1, the intensity of specific transitions at 1550 nm is approx. 3-5 times higher after the processing, which confirms the improved collection efficiency despite a relatively simple photonic microstructure. The spectra are taken for the same excitation power measured in front of the microscope objective, while we observe even more emission lines due to enhanced extraction. They can also origin from the neighboring dots even if they not positioned perfectly in the middle of the mesa. At this dots' density we still can have around 3 dots in the 100×100 nm^2 of the central area. Considering the QD2 case, the spectra show no pronounced emission lines in the 1550 ± 1.5 nm range which is consistent with no signature of emission in Fig. 5(c). Although some background emission of each QD inherently related to phonon coupling or higher order excitonic states typically gives some features on the PL map (low-intensity spectral profile is integrated, which generates detectable counts with high-sensitivity 2D camera chip on a small region of interest), we can eliminate this effectively by adjusting the signal-to-background ratio as a threshold for data visualization to preselect only the dots with pronounced emission lines. We suspect that the positioning accuracy can be improved with a better design of alignment marks, while the control of the FIB processing typically has high accuracy and might not be a critical issue here. Last, the deterministic processing approach is generally required for scalable fabrication purposes, and our results verify its high impact.

6. Conclusions

In this study, we have shown the unique potential of Xe-PFIB in the manufacturing process of photonic structures, particularly in the prototyping of quantum photonic devices. Our use of this cutting-edge technology has allowed fabricating non-deterministic and deterministic mesa structures with a truncated cone shape, featuring enhanced photon extraction efficiency from a single photon emitter operating near 1550 nm, which emitter comprises a self-assembled InAs/InP quantum dot in a hybrid structure all integrated with the silicon platform. We have presented FDTD simulations, which indicate a significantly elevated photon extraction efficiency for such geometries, exceeding 0.6 in the broad wavelength range between 1.50 to 1.58 μm with the peak efficiency of approx. 0.9 (for NA = 0.65). The experiment provided extraction efficiency of 24±4% for the same numerical aperture, which is lower than the calculated, due to possible non-ideal emitter position, but still state-of-the-art for QDs emitting in the third telecom window. The QD-based single photon source fabricated through the process exhibited high emission purity, as evidenced by the $g^{(2)}(0)$ values of $0.04^{+0.08}_{-0.04}$.and $0.01^{+0.03}_{-0.01}$ under continuous wave and pulsed excitation, respectively.

Eventually, we have shown that Xe-PFIB technology can be effectively combined with fast PL imaging of self-assembled quantum dot structures to create photonic devices deterministically. A pre-selected InAs/InP quantum dot emitting at 1550 nm in a mesa structure, displayed a 3-fold increase in emission intensity compared to the unpatterned structure.

Funding. Horizon 2020 Framework Programme (101135785); Danmarks Grundforskningsfond (DNRF147); Ministerstwo Edukacji i Nauki (DWD/4/50/2020); Narodowe Centrum Nauki (2019/33/B/ST5/02941); Narodowe Centrum Nauki (2020/39/D/ST5/02952).

Acknowledgements. This work has been supported by the "Implementation doctorate" program of the Polish Ministry of Education and Science within grant No. DWD/4/50/2020, the grants no. 2019/33/B/ST5/02941 of OPUS17 call and 2020/39/D/ST5/02952 of SONATA16 call of the National Science Centre in Poland, Danish National Research Foundation via Research Centre of Excellence NanoPhoton (Ref. DNRF147) and by European Union's Horizon Europe Research and Innovation Programme under QPIC 1550 project (Grant Agreement No 101135785).

Disclosures. The authors declare no conflicts of interest.

Data availability. Data underlying the results presented in this paper are not publicly available at this time but may be obtained from the authors upon reasonable request.

References

1. P. Senellart, G. S. Solomon, and A. White, "High-performance semiconductor quantum-dot single-photon sources," Nat. Nanotechnol. **12**(11), 1026–1039 (2017).
2. B. Naydenov and F. Jelezko, "Single-color centers in diamond as single-photon sources and quantum sensors," in: 2014 303–318.
3. D. B. Higginbottom, L. Slodička, G. Araneda, *et al.*, "Pure single photons from a trapped atom source," New J. Phys. **18**(9), 093038 (2016).
4. P. Mrowiński, A.J. Musiał, K. Gawarecki, *et al.*, "Excitonic complexes in MOCVD-grown InGaAs/GaAs quantum dots emitting at telecom wavelengths," Phys. Rev. B **100**(11), 115310 (2019).
5. C. Nawrath, F. Olbrich, M. Paul, *et al.*, "Coherence and indistinguishability of highly pure single photons from non-resonantly and resonantly excited telecom C-band quantum dots," Appl. Phys. Lett. **115**(2), 023103 (2019).
6. M. Benyoucef, M. Yacob, J. P. Reithmaier, *et al.*, "Telecom-wavelength (1.5 μm) single-photon emission from InP-based quantum dots," Appl. Phys. Lett. **103**(16), 162101 (2013).
7. A. J. Musiał, K. Żołnacz, N. Srocka, *et al.*, "Plug & play fiber-coupled 73 kHz single-photon source operating in the telecom O-band," Adv. Quantum Technol. **3**(6), 2000018 (2020).
8. E.S. Semenova, R. Hostein, G. Patriarche, *et al.*, "Metamorphic approach to single quantum dot emission at 1.55μm on GaAs substrate," J Appl Phys **103**(10), 103533 (2008).
9. M. Mueller, S. Bounouar, K. D. Jöns, *et al.*, "On-demand generation of indistinguishable polarization-entangled photon pairs," Nat Photon **8**(9), 224–228 (2014).
10. C. Nawrath, R. Joos, S. Kolatschek, *et al.*, "Bright source of purcell-enhanced, triggered, single photons in the telecom C-band," Adv. Quantum Technol. **6**(11), 2300111 (2023).
11. A. Delgoffe, A. Miranda, A. Lyasota, *et al.*, "Integrated quantum photonics using site-controlled quantum dots and tailored-potential photonic crystals," in: *Conference on Lasers and Electro-Optics*, OSA, Washington, D.C., 2019: p. FTh3D.3.
12. P. Schnauber, A. Singh, J. Schall, *et al.*, "Indistinguishable photons from deterministically integrated single quantum dots in heterogeneous GaAs/Si3N4 quantum photonic circuits," Nano Lett. **19**(10), 7164–7172 (2019).
13. J. Liu, M. I. Davanço, L. Sapienza, *et al.*, "Cryogenic photoluminescence imaging system for nanoscale positioning of single quantum emitters," Rev. Sci. Instrum. **88**(2), 023116 (2017).
14. P. Holewa, D. A. Vajner, E. Zięba-Ostój, *et al.*, "High-throughput quantum photonic devices emitting indistinguishable photons in the telecom C-band," Nat. Commun. **15**(1), 3358 (2024).
15. C. Couteau, S. Barz, T. Durt, *et al.*, "Applications of single photons to quantum communication and computing," Nat. Rev. Phys. **5**(6), 326–338 (2023).
16. S. Rodt and S. Reitzenstein, "Integrated nanophotonics for the development of fully functional quantum circuits based on on-demand single-photon emitters," APL Photonics **6**(1), 010901 (2021).
17. T. Kupko, M. von Helversen, L. Rickert, *et al.*, "Tools for the performance optimization of single-photon quantum key distribution," Npj Quantum Inf **6**(1), 29 (2020).

18. M. Bozzio, M. Vyvlecka, M. Cosacchi, *et al.*, "Enhancing quantum cryptography with quantum dot single-photon sources," Npj Quantum Inf **8**(1), 104 (2022).
19. T. Heindel, J.-H. Kim, N. Gregersen, *et al.*, "Quantum dots for photonic quantum information technology," Adv. Opt. Photon. **15**(3), 613 (2023).
20. L. Sapienza, M. I. Davanço, A. Badolato, *et al.*, "Nanoscale optical positioning of single quantum dots for bright and pure single-photon emission," Nat. Commun. **6**(1), 7833 (2015).
21. S. Kolatschek, C. Nawrath, S. Bauer, *et al.*, "Bright Purcell enhanced single-photon source in the telecom O-band based on a quantum dot in a circular Bragg grating," Nano Lett. **21**(18), 7740–7745 (2021).
22. A. J. Musiał, M. Mikulicz, P. Mrowiński, *et al.*, "InP-based single-photon sources operating at telecom C-band with increased extraction efficiency," Appl. Phys. Lett. **118**(22), 1–6 (2021).
23. Ł. Dusanowski, M. Syperek, P. Mrowiński, *et al.*, "Single photon emission at 1.55 μ m from charged and neutral exciton confined in a single quantum dash," Appl. Phys. Lett. **105**(2), 021909 (2014).
24. T. Miyazawa, K. Takemoto, Y. Nambu, *et al.*, "Single-photon emission at 1.5 um from an InAs/InP quantum dot with highly suppressed multi-photon emission probabilities," Appl. Phys. Lett. **109**(13), 132106 (2016).
25. Y. Berdnikov, P. Holewa, S. Kadkhodazadeh, *et al.*, "Fine-tunable near-critical Stranski-Krastanov growth of InAs/InP quantum dots," (2023).
26. M. Schmidt, M. V. Helversen, S. Fischbach, *et al.*, "Deterministically fabricated spectrally-tunable quantum dot based single-photon source," Opt. Mater. Express **10**(1), 76 (2020).
27. M. Horák, K. Bukvišová, V. Švarc, *et al.*, "Comparative study of plasmonic antennas fabricated by electron beam and focused ion beam lithography," Sci. Rep. **8**(1), 9640 (2018).
28. M. Jaworski, A. Chudzyńska, P. Mrowiński, *et al.*, "Xenon-plasma focused ion beam processing of photonic microstructures with GaAs-based quantum dots," Opt. Mater. Express **13**(10), 2845 (2023).
29. C. Rothfuchs, F. Semond, M. Portail, *et al.*, "Ion-induced interdiffusion of surface GaN quantum dots," Nucl. Instrum. Methods Phys. Res., Sect. B **409**, 107–110 (2017).
30. Z. Song, S. Loh, S. Neo, *et al.*, "Application of FIB circuit edit and electrical characterization in failure analysis for invisible defect issues," in: *13th International Symposium on the Physical and Failure Analysis of Integrated Circuits*, IEEE, 2006: pp. 187–191.
31. A. Delobbe, O. Salord, T. Hrncir, *et al.*, "High speed TEM sample preparation by Xe FIB," Microsc. Microanal. **20**(S3), 298–299 (2014).
32. C. Vieu, J. Gierak, M. Schneider, *et al.*, "Evidence of depth and lateral diffusion of defects during focused ion beam implantation," J. Vac. Sci. Technol., B: Microelectron. Nanometer Struct.–Process., Meas., Phenom. **16**(4), 1919–1927 (1998).
33. W. Pacuski, T. Jakubczyk, C. Kruse, *et al.*, "Micropillar cavity containing a CdTe quantum dot with a single manganese ion," Cryst. Growth Des. **14**(3), 988–992 (2014).
34. Y.-L. D. Ho, R. Gibson, C. Y. Hu, *et al.*, "Focused ion beam etching for the fabrication of micropillar microcavities made of III-V semiconductor materials," J. Vac. Sci. Technol., B: Microelectron. Nanometer Struct.–Process., Meas., Phenom. **25**(4), 1197–1202 (2007).
35. M. M. V. Taklo, A. Klumpp, P. Ramm, *et al.*, "Bonding and TSV in 3D IC integration: physical analysis with plasma FIB," Microscopy and Analysis 114 (2011).
36. T. Sato, K. Nakano, H. Matsumoto, *et al.*, "High quality lamella preparation of gallium nitride compound semiconductor using Triple Beam$^{\mathrm{TM}}$ system," J. Phys.: Conf. Ser. **902**, 012019 (2017).
37. L.A. Giannuzzi and F.A. Stevie, eds., *Introduction to Focused Ion Beams*, Springer US, Boston, MA, 2005.
38. M. M. V. Taklo, A. Klumpp, P. Ramm, *et al.*, "Bonding and TSV in 3D IC Integration: Physical Analysis with a Plasma FIB," Microscopy and Analysis **25**, 9–12 (2011).
39. M. Jaworski, A. Chudzyńska, and P. Mrowiński, "Sęk, Efficient emission in the telecom range from quantum dots embedded in photonic structures fabricated by focused ion beam milling," Acta Phys. Pol. A **142**(5), 662–667 (2022).
40. T. Heindel, A. Thoma, M. Von Helversen, *et al.*, "A bright triggered twin-photon source in the solid state," Nat. Commun. **8**(1), 14870 (2017).
41. M. Sartison, L. Engel, S. Kolatschek, *et al.*, "Deterministic integration and optical characterization of telecom O-band quantum dots embedded into wet-chemically etched Gaussian-shaped microlenses," Appl. Phys. Lett. **113**(3), 032103 (2018).
42. M. Gschrey, A. Thoma, P. Schnauber, *et al.*, "Highly indistinguishable photons from deterministic quantum-dot microlenses utilizing three-dimensional in situ electron-beam lithography," Nat. Commun. **6**(1), 7662 (2015).
43. P. Mrowiński and G. Sęk, "Modelling the enhancement of spectrally broadband extraction efficiency of emission from single InAs/InP quantum dots at telecommunication wavelengths," Phys. B (Amsterdam, Neth.) **562**, 141–147 (2019).
44. J. Liu, R. Su, Y. Wei, *et al.*, "A solid-state source of strongly entangled photon pairs with high brightness and indistinguishability," Nat. Nanotechnol. **14**(6), 586–593 (2019).
45. S. Ates, S. M. Ulrich, A. Ulhaq, *et al.*, "Non-resonant dot-cavity coupling and its applications in resonant quantum dot spectroscopy," Nat. Photonics **3**(12), 724–728 (2009).
46. P. Mrowiński, M. Zieliński, M. Świderski, *et al.*, "Excitonic fine structure and binding energies of excitonic complexes in single InAs quantum dashes," Phys. Rev. B **94**(11), 115434 (2016).

47. N. I. Cade, H. Gotoh, H. Kamada, *et al.*, "Fine structure and magneto-optics of exciton, trion, and charged biexciton states in single InAs quantum dots emitting at 1.3 μm," Phys. Rev. B **73**(11), 115322 (2006).
48. E. Dekel, D. Gershoni, E. Ehrenfreund, *et al.*, "Carrier-carrier correlations in an optically excited single semiconductor quantum dot," Physical Review B **61**(16), 9–20 (2000).
49. G. Sęk, A. J. Musiał, P. J. Podemski, *et al.*, "On the applicability of a few level rate equation model to the determination of exciton versus biexciton kinetics in quasi-zero-dimensional structures," J Appl Phys **108**(3), 033507 (2010).
50. C. Becher, A. Kiraz, P. Michler, *et al.*, "Nonclassical radiation from a single self-assembled InAs quantum dot," Phys. Rev. B **63**(12), 121312 (2001).
51. S. Stobbe, J. Johansen, P. T. Kristensen, *et al.*, "Frequency dependence of the radiative decay rate of excitons in self-assembled quantum dots: Experiment and theory," Phys. Rev. B **80**(15), 155307 (2009).
52. F. Albert, S. Stobbe, C. Schneider, *et al.*, "Quantum efficiency and oscillator strength of site-controlled InAs quantum dots," Appl. Phys. Lett. **96**(15), 1746 (2010).
53. Z. Ge, T. Chung, Y.-M. He, *et al.*, "Polarized and bright telecom C-band single-photon source from InP-based quantum dots coupled to elliptical Bragg gratings," Nano Lett. **24**(5), 1746–1752 (2024).
54. M. Syperek, M. Baranowski, G. Sęk, *et al.*, "Impact of wetting-layer density of states on the carrier relaxation process in low indium content self-assembled (In,Ga)As/GaAs quantum dots," Phys. Rev. B **87**(12), 125305 (2013).
55. P. Holewa, M. Gawełczyk, C. Ciostek, *et al.*, "Optical and electronic properties of low-density InAs/InP quantum-dot-like structures designed for single-photon emitters at telecom wavelengths," Phys. Rev. B **101**(19), 195304 (2020).
56. P. Holewa, M. Gawełczyk, A. Maryński, *et al.*, "Optical and electronic properties of symmetric InAs/(In,Al,Ga)As/InP quantum dots formed by ripening in molecular beam epitaxy: a potential system for broad-range single-photon telecom emitters," Phys. Rev. Applied **14**(6), 064054 (2020).